Massively Parallel Modeling and Inversion of Electrical Resistivity Tomography data using PFLOTRAN

Piyoosh Jaysaval, Glenn E. Hammond, and Timothy C. Johnson

Pacific Northwest National Laboratory, 902 Battelle Blvd., Richland, WA 99352, USA

Correspondence: Piyoosh Jaysaval (piyoosh.jaysaval@pnnl.gov)

Abstract.

Electrical resistivity tomography (ERT) is a broadly accepted geophysical method for subsurface investigations. Interpretation of field ERT data usually requires the application of computationally intensive forward modeling and inversion algorithms. For large-scale ERT data, the efficiency of these algorithms depends on the robustness, accuracy, and scalability on high performance computing resources. In this regard, we present a robust and highly scalable implementation of forward modeling and inversion algorithms for ERT data. The implementation is publicly available and developed within the framework of PFLOTRAN, an open-source, state-of-the-art massively parallel subsurface flow and transport simulation code. The forward modeling is based on a finite volume discretization of the governing differential equations, and the inversion uses a Gauss–Newton optimization scheme. To evaluate the accuracy of the forward modeling, two examples are first presented by considering layered (1D) and 3D earth conductivity models. The computed numerical results show good agreement with the analytical solutions for the layered earth model and results from a well-established code for the 3D model. Inversion of ERT data, simulated for a 3D model, is then performed to demonstrate the inversion capability by recovering the conductivity of the model. To demonstrate the parallel performance of PFLOTRAN's ERT process model and inversion capabilities, large-scale scalability tests are performed by using up to $131,072$ processes on a leadership class supercomputer. These tests are performed for the two most computationally intensive steps of the ERT inversion: forward modeling and Jacobian computation. For the forward modeling, we consider models with up to 122 million degrees of freedom in the resulting system of linear equations, and demonstrate that the code exhibits almost linear scalability on up to $8,192$ cores. On the other hand, the code shows perfectly linear scalability for the Jacobian computation, mainly because all computations are fairly evenly distributed over each core with no parallel communication.

1 Introduction

Direct current electrical resistivity tomography (ERT) is one of the oldest and key geophysical methods for shallow-subsurface investigations, having applications in areas such as groundwater (Dahlin, 2001; Johnson et al., 2012; Meyerhoff et al., 2014; Park et al., 2016; Greggio et al., 2018; Alshehri and Abdelrahman, 2021), mineral exploration (Badmus and Olatinsu, 2009; Bery et al., 2012; Uhlemann et al., 2018; Martínez et al., 2019), environmental monitoring and remediation (Rosales et al., 2012; Rucker et al., 2013; Gabarrón et al., 2020; Rockhold et al., 2020; Kessouri et al., 2022), and engineering problems

(Dahlin, 1996; Rizzo et al., 2004; Lysdahl et al., 2017). It can also be used for few large-scale deep-subsurface investigations, e.g., for geothermal systems, active volcano imaging, and tectonic studies (Storz et al., 2000; Caputo et al., 2003; Johnson et al., 2010; Richards et al., 2010). Additional applications can also be found in detailed reviews by Slater (2007), Revil et al. (2012), Loke et al. (2013), Singha et al. (2022), and the references therein. In recent years, availability of multielectrode and multichannel instrumentations permitted acquisition of massive amounts of ERT data consisting of tens of thousands or even hundreds of thousands of observations. Therefore, efficient inversion and interpretation of such massive datasets requires fast, accurate, and highly scalable forward modeling and inversion algorithms to simulate and invert ERT data in arbitrary 3D conductivity structures. This paper presents an open-source implementation of such ERT modeling and inversion algorithms.

ERT data simulation is performed by solving the electrostatic Poisson equation. Numerical methods are often needed to solve the governing equation in arbitrary 3D conductivity structures. The most used numerical methods for 3D ERT modeling are the finite-difference (FD) method (Dey and Morrison, 1979; Spitzer, 1995; Penz et al., 2013), finite-element (FE) method (Coggon, 1971; Li and Spitzer, 2002; Rücker et al., 2006; Blome et al., 2009; Johnson et al., 2010; Ren et al., 2018), and integral equation method (Lee, 1975; Schulz, 1985; Méndez-Delgado et al., 1999). Among these methods, the FD and FE methods are the attractive choices for highly heterogeneous distributions of electrical conductivity in the subsurface. However, application of the FD method is mostly limited to simple model geometries. On the contrary, the FE method has proven to be effective in accounting for complex geometries, specifically by using unstructured meshes (Rücker et al., 2006; Blome et al., 2009; Johnson et al., 2010; Ren et al., 2018).

There is another class of numerical methods, the finite-volume (FV) method, which can also be used effectively to account for complex geometries (Jahandari and Farquharson, 2014). The FV method is usually seen relatively close to the FD method as it inherits the simplicity similar to the FD method in its implementation. Unlike the FD method which discretizes the differential form of the governing equation, the FV method, however, directly discretizes its integral form. Nevertheless, the FV method has rarely been considered for ERT simulation problems. In our literature search, we came across only Cockett et al. (2015) which implements the method for the ERT modeling.

On the other hand, ERT data inversion is a non-linear optimization problem to minimize a cost function that represents a measure of the difference between observed and simulated ERT data. For large-scale 3D ERT data, the inversion is often performed iteratively by linearizing the optimization problem at each iteration, calculating a model update, updating a conductivity model, and subsequently simulating ERT data for the updated model to examine the new cost function. The processes continue until the cost function reduces to a predefined tolerance level. The model update is typically calculated using a gradient-based local optimization method, e.g., the steepest-descent, conjugate gradient, or Gauss–Newton method (Park and Van, 1991; Ellis and Oldenburg, 1994; Zhdanov and Keller, 1994; Zhang et al., 1995; Günther et al., 2006; Johnson et al., 2010). The Gauss–Newton method has usually been preferred due to its high convergence rate. Indeed, the fast convergence occurs at the cost of intensive computations because the method requires building the Jacobian (or sensitivity) and/or Hessian matrices at each inversion iteration (Nocedal and Wright, 2006).

For large-scale 3D ERT data, forward modeling and inversion are computationally demanding jobs and may need hours, if not days, of computing time if the underlying algorithms are not properly implemented to scale well on high performance

computing (HPC) resources or supercomputers. For such datasets, it is computationally infeasible to use desktop based ERT data processing software without exploiting HPC resources. Recently, a few open-source 3D ERT modeling and inversion codes have been developed to handle moderate sized ERT data, e.g., ResIPy (Blanchy et al., 2020), SimPEG (Cockett et al., 2015), and pyGIMLI (Rücker et al., 2017). However, these codes still lack full-scale parallel implementations to efficiently

65 distribute computations over supercomputers. On the other hand, another open-source code, E4D, is highly scalable on HPC resources (Johnson et al., 2010; Johnson and Wellman, 2015). It can be run on hundreds or even thousands of computing cores of a supercomputer (Johnson et al., 2010). But despite this, the maximum number of computing cores that it can exploit is limited to the number of electrodes in a survey.

In this paper, we present an open-source implementation of massively parallel 3D ERT modeling and inversion algorithms.

70 The forward modeling is based on the FV method and inversion employs the Gauss–Newton method. The computations are parallelized so that all available HPC resources can be exploited, provided they are beneficial. The algorithms are implemented within the framework of PFLOTRAN (https://pflotran.org) which is an open-source, state-of-the-art massively parallel subsurface flow and transport simulation code and has been used extensively for various subsurface applications (Hammond et al., 2012, 2014). Although we are presenting only the ERT modeling and inversion capabilities here, the main motivation of im-

75 plementing these capabilities in PFLOTRAN is to perform coupled modeling and inversion of ERT, flow, and/or transport problems.

The paper is structured as follows: we first outline a detailed background theory on the ERT forward modeling including the governing Poisson equation and FV method to solve it numerically. We then describe the ERT inversion by defining it as a nonlinear optimization problem, and the Gauss–Newton method to find a minimizer of the problem along with details on

80 computing the Jacobian matrix. Thereafter, we discuss the parallel implementations of the modeling and inversion algorithms. We subsequently benchmark numerical results computed using PFLOTRAN against analytical solutions for a layered (1D) earth model and numerical solutions for a 3D earth model. Next, a 3D inversion result is presented to illustrate the inversion capability. Scalability tests are then performed to demonstrate the parallel performance of the PFLOTRAN ERT process model, before drawing our final concluding remarks.

85   2 Forward modeling

Forward modeling is a way of simulating ERT data for any given 1D, 2D, or 3D electrical conductivity models of the earth. For 1D conductivity models, the electrical potentials generated by an induced point current source can be obtained by using analytical or semi-analytical methods (Das, 1995; Pervago et al., 2006). However, for multi-dimensional heterogeneous conductivity models with complex geometries, one must use numerical methods to compute the electrical potential. This section

90 describes the numerical computations of the electrical potentials in a 3D medium and their superposition to produce simulated ERT data.

2.1 Poisson's equation

The ERT forward modeling is governed by the following electrostatic Poisson equation

$$\boldsymbol{\nabla} \cdot \sigma(\mathbf{r}) \boldsymbol{\nabla} \phi(\mathbf{r}) = -I\delta(\mathbf{r} - \mathbf{r}_\mathrm{s}), \tag{1}$$

95 where ϕ is the electrical potential at position $\mathbf{r}$ for a given conductivity $\sigma(\mathbf{r})$ due to a current I injected through a point located at $\mathbf{r}_\mathrm{s}$; and δ is the Dirac delta function. For brevity, hereinafter, the dependencies on $\mathbf{r}$ will be omitted except where necessary to show.

If side and bottom boundaries $\partial\Gamma$ of the 3D computational domain Γ are located at sufficiently far from the current injection location $\mathbf{r}_\mathrm{s}$, the potential and the normal component of the current density $\sigma\frac{\partial\phi}{\partial n}$ asymptotically approach zero. On the top or
100 surface boundary $\partial\Gamma_\mathrm{S}$, the normal current density $\sigma\frac{\partial\phi}{\partial n}$ is zero as no current flows through the earth surface along the outward normal vector. Consequently, we can impose zero Dirichlet or Neumann boundary conditions at the side boundaries and zero Neumann boundary at the surface boundary

$$\phi|_{\partial\Gamma} = 0 \quad \text{or} \quad \frac{\partial\phi}{\partial n}|_{\partial\Gamma} = 0, \quad \text{and} \quad \frac{\partial\phi}{\partial n}|_{\partial\Gamma_\mathrm{S}} = 0. \tag{2}$$

To simulate ϕ in arbitrary 3D conductivity structures, Eq. (1) needs to be solved using numerical methods subject to the
105 boundary conditions in Eq. (2).

2.2 Finite volume method

The FV method is implemented to compute ϕ by solving Eq. (1). The 3D computational domain is first discretized into a set of control volumes knows as cells (Fig. 1). These cells can be of arbitrary shape and size, but they must be bounded by planar surfaces for our implementation. The bounding discrete surfaces are known as cell faces.
110 Let us consider the governing Poisson equation (Eq. 1) and integrate it over the ith cell of the domain Γ. This gives

$$\int_{V_i} \boldsymbol{\nabla} \cdot \sigma \boldsymbol{\nabla} \phi \, dV = -\int_{V_i} I\delta(\mathbf{r} - \mathbf{r}_\mathrm{s}) \, dV, \tag{3}$$

where V_i is the volume of the ith cell.

By applying the Gauss divergence theorem in Eq. (3) and using the translation property of the Dirac delta function, we get

$$\int_{S_i} \sigma \boldsymbol{\nabla} \phi \cdot \hat{\mathbf{n}} \, dS = -I|_{\mathbf{r}=\mathbf{r}_\mathrm{s}}, \tag{4}$$

115 where S_i is the surface area of the bounding faces of ith cell, and dS is a differential area on the bounding surface with a unit surface normal $\hat{\mathbf{n}}$ pointing outward.
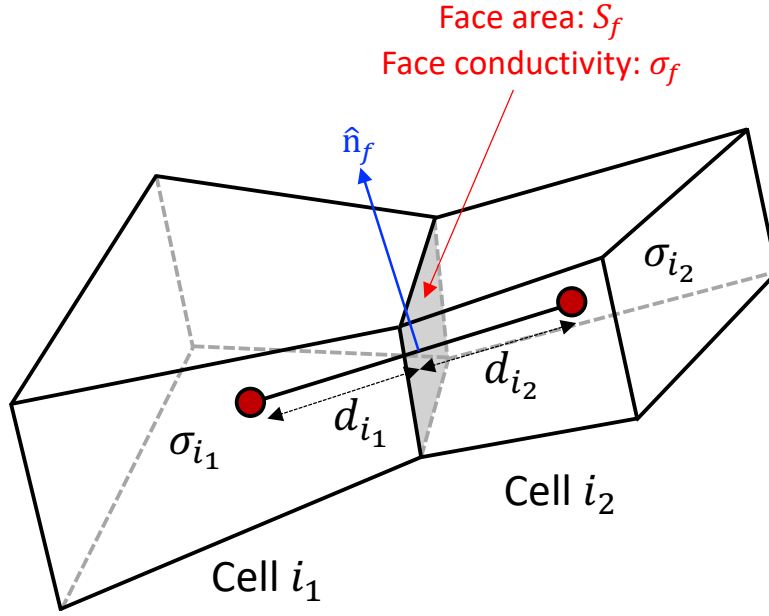
Figure 1. Two adjacent FV cells i_1 and i_2 having conductivity σ_{i_1} and σ_{i_2}, respectively. The distances of the common face f from the center of cells i_1 and i_1, respectively, are d_{i_1} and d_{i_2}.

If the ith cell is bounded by N_{f} faces, Eq. (4) can be replaced by an equivalent discrete form

$$\sum_{f=1}^{N_{\mathrm{f}},i} \int_{S_f} \sigma \boldsymbol{\nabla}\phi \cdot \hat{\mathbf{n}}\, dS = \sum_{f=1}^{N_{\mathrm{f}},i} \sigma_f (\boldsymbol{\nabla}\phi)_f \cdot \hat{\mathbf{n}}_f\, S_f = -I|_{\mathbf{r}=\mathbf{r}_{\mathrm{s}}}, \tag{5}$$

where f represents faces and S_f is the area of the bounding face f.

120   Using a two-point flux approximation for each face term in Eq. (5) by considering two adjacent cells i_1 and i_2 shown in Fig. 1, we get

$$\sum_{f=1}^{N_{\mathrm{f}},i} \sigma_f (\boldsymbol{\nabla}\phi)_f\, S_{nf} = -I|_{\mathbf{r}=\mathbf{r}_{\mathrm{s}}}, \tag{6}$$

where S_{nf} is the area of the common face f projected onto the plane normal to the vector connecting centers of cells i_1 and i_2.

125   The conductivity at the face, σ_f, can be obtained by averaging the conductivity of cells i_1 and i_2. We use the following harmonic distance weighted scheme to calculate σ_f

$$\sigma_f = \frac{\sigma_{i_1}\sigma_{i_2}(d_{i_1}+d_{i_2})}{\sigma_{i_1}d_{i_2}+\sigma_{i_2}d_{i_1}},\tag{7}$$

where σ_{i_1} and σ_{i_2} are the conductivities of cells i_1 and i_2, and d_{i_1} and d_{i_2} are the distances of the projected face from the center of cells i_1 and i_1, respectively (Fig. 1).

130   The value of the flux at the face f, i.e., $(\boldsymbol{\nabla}\phi)_f$, is obtained by using the approximation

$$(\boldsymbol{\nabla}\phi)_f = \frac{\phi_{i_2}-\phi_{i_1}}{d_{i_1}+d_{i_2}}.\tag{8}$$

Substituting Eqs. (7) and (8) in Eq. (6), and assuming that the computational domain Γ is subdivided into N_{m} FV cells, i.e., $\Gamma = \cup_{i=1}^{N_{\mathrm{m}}}\Gamma^i$ where $\Gamma^i \subset \mathbb{R}^3$ is the ith cell domain, we have

$$\sum_{i=1}^{N_{\mathrm{m}}} A_{i,k}\phi_k = s_i,\tag{9}$$

135   where $A_{i,k}$ is the local coefficient matrix and s_i is the source vector for the ith cell.

The assembly of the local coefficient matrix into a global system, upon carrying out the summation in Eq. (9), results into the system of linear equations

$$\mathbf{A}\boldsymbol{\Phi} = \mathbf{s},\tag{10}$$

where $\mathbf{A} \in \mathbb{R}^{N_{\mathrm{m}}\times N_{\mathrm{m}}}$ is the symmetric system matrix resulting from the FV discretization of Eq. (1), $\boldsymbol{\Phi} \in \mathbb{R}^{N_{\mathrm{m}}}$ is a vector
140   containing the unknown electric potential for all cells, and $\mathbf{s} \in \mathbb{R}^{N_{\mathrm{m}}}$ is the source vector resulting from the right-hand side of Eq. (1). To solve this linear system, we utilize various options of iterative solvers available from PETSc (Portable, Extensible Toolkit for Scientific Computation) (Balay et al., 2021). Each electrode in an ERT survey results in a different vector $\mathbf{s}$. Thus, for N_{e} electrodes, we need to solve Eq. (10) for N_{e} times with a different right-hand side. The solutions provide electrical potential at each cell center of the discrete computational domain and for each current injection location. Finally, the potential
145   distribution for any combination of source/sink electrodes can be obtained by subtracting the potential associated with the sink electrodes from the source electrodes potential (Johnson et al., 2010).

3   Inversion

ERT Inversion is a procedure of estimating electrical conductivity of the earth from a set of observed ERT data and/or some imposed constraints. The ERT inverse problem is a non-linear optimization problem. For large-scale 3D ERT data, the inversion

is often performed iteratively by linearizing the problem at each iteration. This section details our approach of performing inversion of ERT data.

3.1 Optimization problem

We pose the inverse problem as a non-linear minimization problem of finding a conductivity model

$$\mathbf{m}_{\text{inv}} = \arg \min_{\mathbf{m} \in \mathbf{M}} \psi(\mathbf{m}), \tag{11}$$

where $\mathbf{m} = (m_1, m_2, ..., m_{N_{\text{m}}})^T$ is an unknown model parameters vector in the model set $\mathbf{M}$. Since the conductivity within subsurface can vary over several order of magnitudes, the inversion operations are performed for logarithmic conductivity, i.e., we assume $\mathbf{m} = \ln \boldsymbol{\sigma}$. This also enforces positivity of conductivity values. The quantity ψ is the cost function, defined as

$$\psi(\mathbf{m}) = \psi_{\text{d}}(\mathbf{m}) + \beta \psi_{\text{m}}(\mathbf{m}), \tag{12}$$

where ψ_{d} is the data cost function that represents a measure of the misfit between the observed d^{obs} and synthetic d^{syn} ERT data; ψ_{m} is the regularization cost function representing a measure of the variation of the model parameters, and β is a regularization parameter.

A least-squares method is used to minimize ψ (Nocedal and Wright, 2006). Thus, ψ_d and ψ_m can be expressed as

$$\psi_{\text{d}} = [\mathbf{d}^{\text{obs}} - \mathbf{d}^{\text{syn}}(\mathbf{m})]^T \mathbf{W}_{\text{d}}^T \mathbf{W}_{\text{d}} [\mathbf{d}^{\text{obs}} - \mathbf{d}^{\text{syn}}(\mathbf{m})], \tag{13}$$

$$\psi_{\text{m}} = (\mathbf{m} - \mathbf{m}_{\text{ref}})^T \mathbf{W}_{\text{m}}^T \mathbf{W}_{\text{m}} (\mathbf{m} - \mathbf{m}_{\text{ref}}), \tag{14}$$

where vectors $\mathbf{d}^{\text{obs}}$ and $\mathbf{d}^{\text{syn}}$ are N_{d} dimensional vectors containing the observed and synthetic ERT data. $\mathbf{W}_{\text{d}} \in \mathbb{R}^{N_{\text{d}} \times N_{\text{d}}}$ is the data weighting matrix, usually a diagonal matrix, whose elements are estimated based on the standard deviation of the noise; $\mathbf{W}_{\text{m}} \in \mathbb{R}^{N_{\text{m}} \times N_{\text{m}}}$ is the regularization matrix, and $\mathbf{m}_{\text{ref}}$ is a N_{m} dimensional vector containing the logarithmic of reference conductivity model parameters.

3.2 Gauss-Newton method

To find a minimizer $\mathbf{m}_{\text{inv}}$ of the cost function in Eq. (12), we use a Gauss-Newton minimization approach. This is an iterative approach where after linearizing $\psi(\mathbf{m}_k)$ in the vicinity of a model $\mathbf{m}_k$ for a small model perturbation $\delta \mathbf{m}_k$ at the kth iteration, we obtain a set of linear equations or the normal equation

$$\boldsymbol{\mathcal{H}}_k \delta \mathbf{m}_k = -\mathbf{g}_k, \tag{15}$$

where the Gauss-Newton Hessian $\boldsymbol{\mathcal{H}}_k \in \mathbb{R}^{N_\mathrm{m} \times N_\mathrm{m}}$ matrix is given by

175
$$\boldsymbol{\mathcal{H}}_k = \mathfrak{Re}\{\boldsymbol{\mathcal{J}}_k^T \mathbf{W}_\mathrm{d}^T \mathbf{W}_\mathrm{d} \boldsymbol{\mathcal{J}}_k\} + \beta \mathbf{W}_\mathrm{m}^T \mathbf{W}_\mathrm{m}, \tag{16}$$

and the gradient vector by

$$\mathbf{g}_k = -\mathfrak{Re}[\boldsymbol{\mathcal{J}}_k^T \mathbf{W}_\mathrm{d}^T \mathbf{W}_\mathrm{d}\{\mathbf{d}^\mathrm{obs} - \mathbf{d}^\mathrm{syn}\}] + \beta \mathbf{W}_\mathrm{m}^T \mathbf{W}_\mathrm{m}\{\mathbf{m}_k - \mathbf{m}_\mathrm{ref}\}. \tag{17}$$

The matrix $\boldsymbol{\mathcal{J}}_k$ is the Jacobian matrix also known as the sensitivity or the Fréchet derivative matrix. Following Johnson et al. (2010), we implement a parallel conjugate-gradient least-square (CGLS) solver (Hestenes and Stiefel, 1952) to solve

180 the normal Eq. (15). The normal equation is first reformulated into an equivalent least-squares problem and then solved for the model update $\delta\mathbf{m}_k$ using only the Jacobian matrix $\boldsymbol{\mathcal{J}}_k$ without explicitly forming the Hessian matrix $\boldsymbol{\mathcal{H}}_k$. As $N_\mathrm{m} \gg N_\mathrm{d}$ for typical ERT surveys, this approach avoids massive computational cost associated with the explicit formation of $\boldsymbol{\mathcal{H}}_k$. We therefore only need to compute $\boldsymbol{\mathcal{J}}_k$ at each iteration, which is also a computationally intensive step. The effective computation of $\boldsymbol{\mathcal{J}}_k$ is explained in the next subsection 3.3.

185 The solution of Eq. (15) gives a model update vector $\delta\mathbf{m}_k$ at the kth iteration such that a new model

$$\mathbf{m}_{k+1} := \mathbf{m}_k + \alpha\delta\mathbf{m}_k \tag{18}$$

decreases the cost function ψ, i.e., $\psi(\mathbf{m}_{k+1}) < \psi(\mathbf{m}_k)$. There is a common practice to find step-length α using a line search method (Nocedal and Wright, 2006); however, from our experience, a full step-length, i.e., $\alpha = 1$, works well for the ERT data inversion.

190 In our implementation, the Gauss-Newton iteration usually starts with an average apparent conductivity model as an initial model and continues until the data misfit drops below a predefined tolerance level (defined by a chi-squared data misfit $\chi^2 = \phi_d/N_\mathrm{d} \le 1$) or it reaches a predefined maximum number of iterations. Furthermore, a predefined input conductivity model can also be used as an initial model in case it can be estimated from the existing geological and/or geophysical information. After the inversion converges, it provides the minimizer $\mathbf{m}_\mathrm{inv}$ which represents the inverted conductivity model $\boldsymbol{\sigma}_\mathrm{inv} = \exp(\mathbf{m}_\mathrm{inv})$.

195 ## 3.3 Jacobian computation

Calculating $\boldsymbol{\mathcal{J}}$ at each iteration is one of the most computationally intensive steps in Gauss-Newton inversion. Therefore, an efficient $\boldsymbol{\mathcal{J}}$ drives the robustness of the developed inversion scheme and maximizes its scalability. The Jacobian matrix characterizes the change in the synthetic ERT data $\mathbf{d}^\mathrm{syn}$ relative to a change in the model parameters $\mathbf{m}$, and is defined as the partial derivatives of $\mathbf{d}^\mathrm{syn}$ with respect to $\mathbf{m} = \ln\boldsymbol{\sigma}$, i.e.,

200 $$\mathcal{J}_{j,k} = \frac{\partial d_j^\mathrm{syn}}{\partial m_k} = \sigma_k \frac{\partial d_j^\mathrm{syn}}{\partial \sigma_k}; \quad j = 1, 2, ..., N_\mathrm{d} \quad \text{and} \quad k = 1, 2, ..., N_\mathrm{m}. \tag{19}$$

An adjoint state method is used to effectively compute the Jacobian matrix. Let A and B be the source and sink electrodes located at $\mathbf{r}_A$ and $\mathbf{r}_B$, and M and N be the two measuring or receiving electrodes located at $\mathbf{r}_M$ and $\mathbf{r}_N$. The potential difference between M and N can be obtained using the potential computed due to the source A at M and N, i.e., ϕ_{AM} and ϕ_{AN}, and the sink B at M and N, i.e., ϕ_{BM} and ϕ_{BN}. A simplified four-electrodes Wenner configuration is shown in Fig. 2. Note that, contrary to this configuration, electrodes can be placed in any other configurations, e.g., Schlumberger, pole-pole, pole-dipole, dipole-dipole, and gradient arrays, among others (Dahlin and Zhou, 2004).
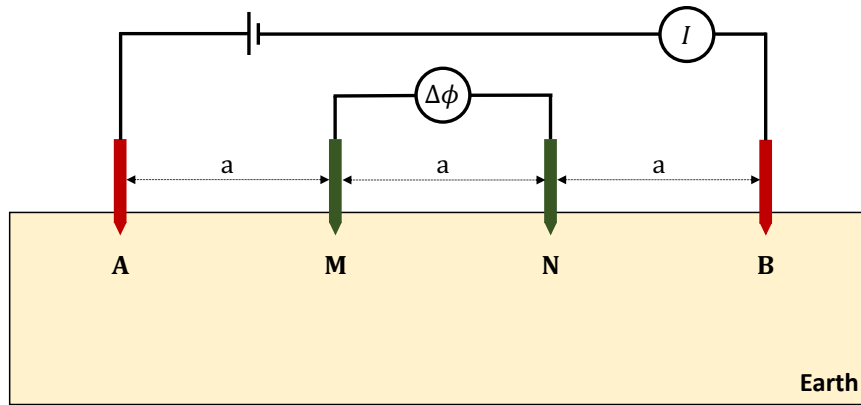
Figure 2. Wenner electrode configuration: four electrodes A, B, M, and N are deployed in-line with an equal spacing a between the two neighboring electrodes. Electrodes A and B act as the source and sink electrodes where current I is injected, while electrodes M and N act as the receiving electrodes measuring a potential difference $\Delta\phi$.

Let's assume that $\mathbf{p}_M$ and $\mathbf{p}_N$ are two interpolation vectors and $\boldsymbol{\Phi}_A$ and $\boldsymbol{\Phi}_B$ are potential distributions due to the source A and sink B such that

$$\phi_{AM} = \mathbf{p}_M^T \boldsymbol{\Phi}_A, \quad \phi_{AN} = \mathbf{p}_N^T \boldsymbol{\Phi}_A, \quad \phi_{BM} = \mathbf{p}_M^T \boldsymbol{\Phi}_B, \quad \text{and} \quad \phi_{BN} = \mathbf{p}_N^T \boldsymbol{\Phi}_B. \tag{20}$$

Therefore, the jth simulated potential difference between the receiving electrodes M and N can be obtained as

$$d_j^{\text{syn}} = \phi_{AM} - \phi_{AN} - \phi_{BM} + \phi_{BN}. \tag{21}$$

Using Eq. (20) in Eq. (21), we get

$$d_j^{\text{syn}} = \mathbf{p}_M^T (\boldsymbol{\Phi}_A - \boldsymbol{\Phi}_B) - \mathbf{p}_N^T (\boldsymbol{\Phi}_A - \boldsymbol{\Phi}_B). \tag{22}$$

Taking derivative of Eq. (22) with respect to conductivity m_k of kth cell yields

$$215 \quad \frac{\partial d_j^{\text{syn}}}{\partial m_k} = \mathbf{p}_M^T \frac{\partial}{\partial m_k}(\boldsymbol{\Phi}_A - \boldsymbol{\Phi}_B) - \mathbf{p}_N^T \frac{\partial}{\partial m_k}(\boldsymbol{\Phi}_A - \boldsymbol{\Phi}_B). \tag{23}$$

Furthermore, taking derivative of Eq. (10) with respect to m_k yields

$$\frac{\partial \mathbf{A}}{\partial m_k}\boldsymbol{\Phi} + \mathbf{A}\frac{\partial \boldsymbol{\Phi}}{\partial m_k} = \mathbf{0}, \tag{24}$$

where we used $\partial \mathbf{s}/\partial m_k = 0$ as the source does not depend on the conductivity.

If $\mathbf{A}$ is invertible, rearranging Eq. (24) gives

$$220 \quad \frac{\partial \boldsymbol{\Phi}}{\partial m_k} = -\mathbf{A}^{-1}\frac{\partial \mathbf{A}}{\partial m_k}\boldsymbol{\Phi}. \tag{25}$$

Using Eq. (25) in Eq. (23), we get

$$\frac{\partial d_j^{\text{syn}}}{\partial m_k} = -\mathbf{p}_M^T \mathbf{A}^{-1}\frac{\partial \mathbf{A}}{\partial m_k}(\boldsymbol{\Phi}_A - \boldsymbol{\Phi}_B) + \mathbf{p}_N^T \mathbf{A}^{-1}\frac{\partial \mathbf{A}}{\partial m_k}(\boldsymbol{\Phi}_A - \boldsymbol{\Phi}_B). \tag{26}$$

As $\partial d_j^{\text{syn}}/\partial m_k$ is a scalar quantity, using the property $\mathbf{x}^T\mathbf{y} = \mathbf{y}^T\mathbf{x}$ for two vectors $\mathbf{x}$ and $\mathbf{y}$, Eq. (26) yields

$$\frac{\partial d_j^{\text{syn}}}{\partial m_k} = -(\boldsymbol{\Phi}_A - \boldsymbol{\Phi}_B)^T \frac{\partial \mathbf{A}}{\partial m_k}(\mathbf{A}^{-1}\mathbf{p}_M - \mathbf{A}^{-1}\mathbf{p}_N), \tag{27}$$

225   where $\mathbf{A}^T = \mathbf{A}$ is used due to its symmetry.

If the same interpolation scheme is used for placing the current electrodes within the discretized cells and recording the potential at electrodes from the cell potentials, we will have $\mathbf{A}^{-1}\mathbf{p}_M = -\boldsymbol{\Phi}_M$ and $\mathbf{A}^{-1}\mathbf{p}_N = -\boldsymbol{\Phi}_N$. Therefore,

$$\frac{\partial d_j^{\text{syn}}}{\partial m_k} = (\boldsymbol{\Phi}_A - \boldsymbol{\Phi}_B)^T \frac{\partial \mathbf{A}}{\partial m_k}(\boldsymbol{\Phi}_M - \boldsymbol{\Phi}_N). \tag{28}$$

Assuming $\boldsymbol{\Phi}_S = \boldsymbol{\Phi}_A - \boldsymbol{\Phi}_B$ and $\boldsymbol{\Phi}_R = \boldsymbol{\Phi}_M - \boldsymbol{\Phi}_N$, where $\boldsymbol{\Phi}_S$ is the net potential due to the source and sink electrodes A and

230   B; and $\boldsymbol{\Phi}_R$ is the net potential due to source and sink assumed to be located, respectively, at the receiving electrodes M and N, this results in

$$\frac{\partial d_j^{\text{syn}}}{\partial m_k} = \boldsymbol{\Phi}_S^T \frac{\partial \mathbf{A}}{\partial m_k}\boldsymbol{\Phi}_R. \tag{29}$$

Equation (29) is valid for any numbers of the source/sink electrodes and the receiving electrodes as well as any of their combinations. One only needs to compute the net potentials due to the source/sink electrodes $\boldsymbol{\Phi}_S$ and receiving electrodes $\boldsymbol{\Phi}_R$

235   using the superposition principle.

4 Parallel implementation

To execute simulations in parallel, domain decomposition is employed to distribute the discrete computational domain across (computer) processes using a logical decomposition along the three principal axes (calculated by PETSc or explicitly defined by the user) for structured grids, or in the case of unstructured grids, the ParMETIS parallel graph partitioner (Karypis and

240 Schloegel, 2013) is employed to divide the domain and maximize load balance. All interprocessor communication is carried out with MPI (Message Passing Interface), and PETSc's parallel data structures facilitate much of the MPI communication.

Efficient partitioning and the overlapping of communication with computation helps improve parallel performance. The goal is to maximize the time spent in computation and minimize interprocessor communication. Efficient partitioning can be accomplished by dividing the domain evenly and minimizing the number and size of (MPI) messages passed between

245 processes.

PFLOTRAN runs most efficiently when at least 10,000 degrees of freedom (DOFs) or unknowns are assigned to each process (Hammond et al., 2014). This 10,000 DOFs threshold applies for PFLOTRAN ERT simulations as each grid cell has a single degree of freedom. For increasingly complicated reactive transport simulations with many DOFs per grid cell, the number of DOFs per process can drop well below 10,000, since the reactive transport problem is more computational demanding (i.e.,

250 many more floating point operations per grid cell), and the linear system of equations (solved in the Newton-Raphson method) are diagonally dominant and easier to precondition using cheap parallel preconditions such as block Jacobi with ILU[0] in each block (Hammond et al., 2005, 2014).

Another factor limiting parallel performance is the scalability of linear Krylov solvers. Mills et al. (2009) demonstrates that the vector inner products (essentially, global reductions) performed within Krylov solvers become increasingly expensive as

255 tens of thousands of processes are employed to solve a problem. As more compute nodes are added to solve the problem on increasing numbers of processes, additional switches within the high-performance communication fabric must be traversed, and each switch introduces additional latency to communication time. Global reductions are known to be latency bound. Mills et al. demonstrates that Krylov solver parallel performance (i.e., scalability) tends to degrade beyond several tens of thousands of processes.

260 No special pre- or post-processing is required to execute a PFLOTRAN simulation in parallel. Parallel file I/O is through HDF5, and the code handles the distribution and collection of all parameters and (serially-defined) datasets to and from the computer processes with the exception of observation points. PFLOTRAN writes observation files locally on each process (if the process owns at least one observation point), appending the process ID to the filename of the ASCII-formatted file.

5 Modeling benchmarking results

265 To examine the accuracy of the PFLOTRAN ERT process model, simulation results are compared against solutions obtained using well established analytical and numerical methods. Two cases are considered for the comparison: three-layer earth and 3-D earth resistivity models. All benchmarking simulations were performed on the Deception Supercomputer housed at the

Pacific Northwest National Laboratory. It is composed of 96 compute nodes where each node has 64-core AMD EPYC 7502 processors running at 2.5 GHz boost to 3.35 GHz with 256 GB of memory.

5.1 Layered earth model

Let us consider the layered earth or 1D model shown in Fig. 3. The model is composed of three layers, whose resistivity (ρ) and thickness (t) are [100 Ωm, 30 m], [300 Ωm, 30 m], and [10 Ωm, half-space], respectively, from the top to bottom. The dimension of the model is $400 \times 400 \times 100$ m^3. The model boundaries are extended to ± 3000 m in the x- and y-directions, and 3000 m in the z-direction to accommodate zero Dirichlet boundary condition at the side and bottom boundaries. These boundary extensions are not shown in Fig. 3. Vertical electrical sounding (VES) data are simulated at the center of the model considering a Wenner configuration. This configuration consists of four electrodes A, B, M, and N, which are deployed in-line with an equal spacing a between the two neighboring electrodes (Fig. 2). Electrodes A and B again act as the current source and sink electrodes, while electrodes M and N as the potential receiving electrodes. Starting with a smaller value of a for a shallow depth investigation, the value is progressively increased to examine deeper depths. In our case, we start with a minimum value $a_{min} = 8$ m and progressively increase it to a maximum $a_{max} = 132$ m following $a = a_{min} + i\delta a$, where $\delta a = 4$ m and $i = 0, 1, 2, ..., 31$. This results in $N_d = 32$ VES sounding recordings using $N_e = 128$ electrodes.
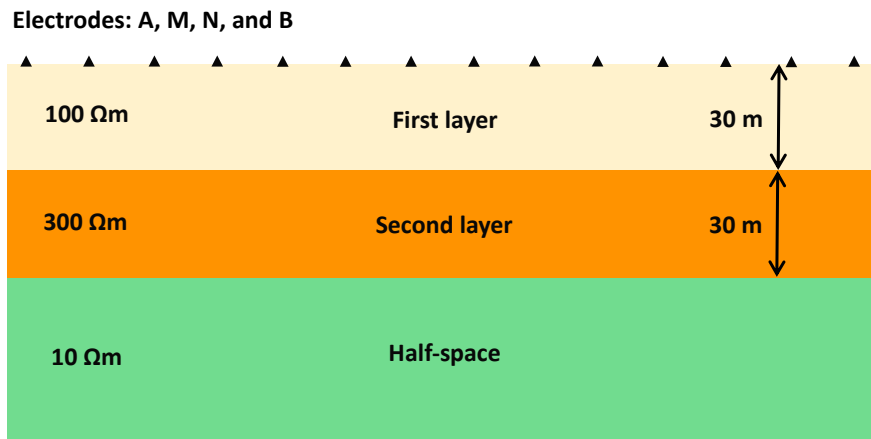
Figure 3. Vertical cross-section of a three-layer earth resistivity model used for benchmarking PFLOTRAN results against the analytical solutions.

To simulate the VES data, the model is discretized using a mix of uniform and non-uniform cell sizes in the x-, y-, and z-directions. The main computational domain is discretized with a uniform grid spacings of 2 m in the x- and y-directions and 1 m in the z-direction. The boundary regions are discretized with severely stretched non-uniform grid spacings following Jaysaval et al. (2014). The discretization results in a grid with $240 \times 240 \times 120$ cells. Therefore, using the FV method to simulate
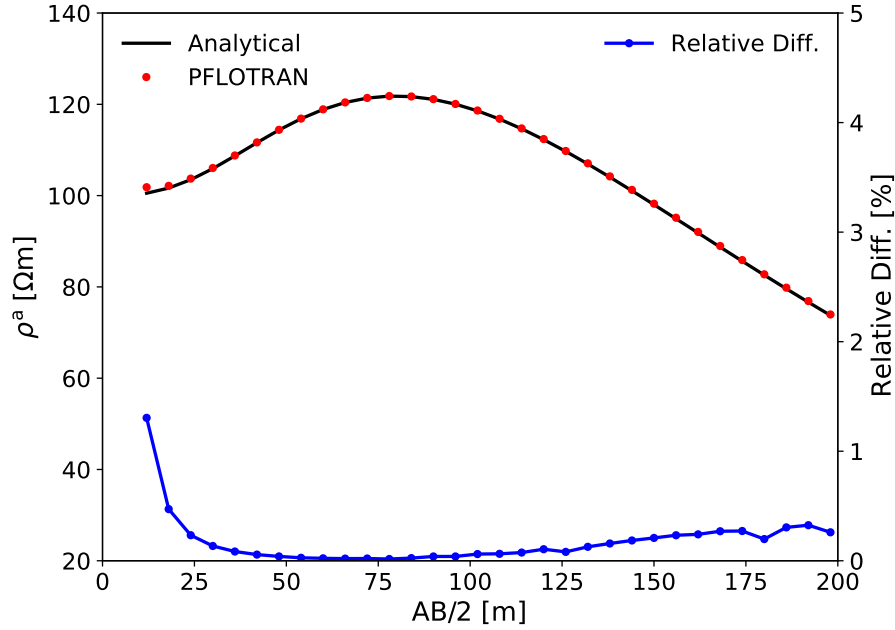
Figure 4. Apparent resistivity ρ^{a} responses computed for the layered earth resistivity model in Fig. 3 (upper plot). They are calculated using the analytical method (solid black lines) and PFLOTRAN (filled red circles). The lower plot (blue line) shows the relative difference (in percentage) between the analytical and PFLOTRAN results.

electric potentials leads to a system of linear equations with $6,912,000$ DOFs. PFLOTRAN simulated the VES data using 512 processing cores on Deception. Total simulation time was $45\,\mathrm{s}$.

The simulated VES results are compared against analytical solutions obtained from SimPEG (Cockett et al., 2015). Figure 4 shows the comparison of the apparent resistivity ρ^{a} responses. Analytical and PFLOTRAN results are shown by the solid

290 black line and filled red circles, respectively. We observe that both responses agree very well with each other. To make the comparison more quantitative, we calculate the relative difference between the two responses and show the difference in Fig. 4 (blue line). The relative difference varies from 0.02% to 1.3%. We also calculate the average relative difference using

$$\epsilon = \frac{1}{N_{\mathrm{d}}} \sum_{i}^{N_{\mathrm{d}}} \frac{\rho^{\mathrm{a}}_{1i} - \rho^{\mathrm{a}}_{2i}}{\rho^{\mathrm{a}}_{1i}}, \tag{30}$$

where ρ^{a} with subscripts 1 and 2, respectively, represents the apparent resistivity computed using PFLOTRAN and the

295 analytical method from SimPEG. The average relative difference ϵ is 0.18%. These relatively small differences demonstrate

the high degree of accuracy of the PFLOTRAN ERT process model for the 1D model. Note that the apparent resistivity was computed using

$$\rho^{\mathrm{a}} = \frac{\Delta \phi}{IG} , \tag{31}$$

where $\Delta \phi = \phi_{\mathrm{AM}} - \phi_{\mathrm{AN}} - \phi_{\mathrm{BM}} + \phi_{\mathrm{BN}}$ and G is a geometric factor given as

300
$$G = \frac{1}{2\pi} \left(\frac{1}{r_{\mathrm{AM}}} - \frac{1}{r_{\mathrm{AN}}} - \frac{1}{r_{\mathrm{BM}}} + \frac{1}{r_{\mathrm{BN}}} \right) , \tag{32}$$

with distances between the source electrode A and the receiving electrodes M and N are, respectively, r_{AM} and r_{AN}, while between the sink electrode B and the receiving electrodes M and N are, respectively, r_{BM} and r_{BN}. For the Wenner configuration, $r_{\mathrm{AM}} = a$, $r_{\mathrm{AN}} = 2a$, $r_{\mathrm{BM}} = 2a$, and $r_{\mathrm{BN}} = a$. Therefore, geometric factor $G = 1/2\pi a$ was used for calculating ρ^{a} using Eq. (31).

305 **5.2   3D earth model**

In the previous example, PFLOTRAN accuracy for simulating ERT responses was validated for a simplistic 1D earth model. In real world, however, the earth models are 3-D with varying degrees of heterogeneity. Therefore, it is important to validate the accuracy of numerical results computed using PFLOTRAN against results computed using well established methods for 3D models.
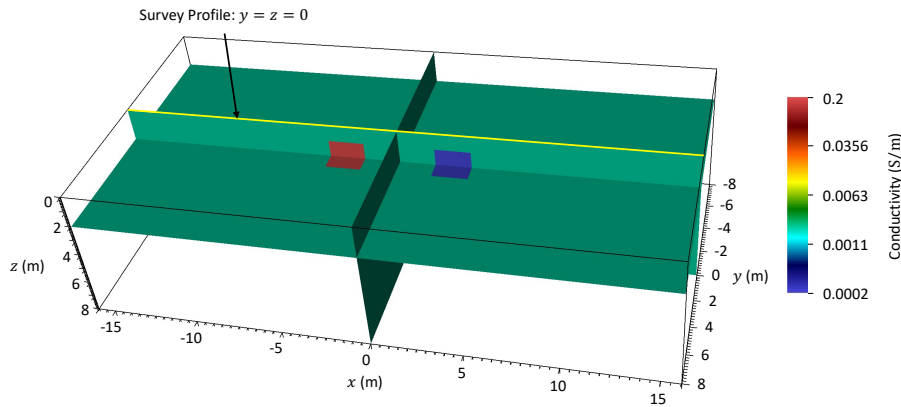
Figure 5. 3D earth resistivity model composed of two anomalous blocks embedded in a homogeneous background. ERT profiling data are simulated along a survey profile at $y = z = 0$ m from $x = -16$ m to $x = 16$ m using the Wenner configuration with increasing electrode spacing a from 1 to 6 m.

310   We consider the 3D model shown in Fig. 5. The model dimension is $32 \times 16 \times 8 \,\mathrm{m}^3$. It has a homogeneous background of conductivity $0.002 \,\mathrm{S m}^{-1}$ and includes two anomalous blocks: a conductivity block $(0.2 \,\mathrm{S m}^{-1})$ and a resistive block

$(0.0002 \, \mathrm{Sm^{-1}})$. Both anomalous blocks have a dimension of $2 \times 2 \times 2 \, \mathrm{m^3}$ and are separated by $4 \, \mathrm{m}$ in the x-direction. As in the previous case, the model boundaries are extended to $\pm 1000 \, \mathrm{m}$ in the x- and y-directions, and $1000 \, \mathrm{m}$ in the z-direction to accommodate zero Dirichlet boundary condition at the side and bottom boundaries. ERT profiling data are simulated along a

315   survey profile (yellow line) at $y = z = 0 \, \mathrm{m}$ from $x = -16 \, \mathrm{m}$ to $x = 16 \, \mathrm{m}$ using the Wenner configuration with increasing electrode spacing a from 1 to $6 \, \mathrm{m}$. Unlike the VES performed for the 1D model where data were simulated at a single observation point at the center of the model, the ERT profiling, performed for the 3D model, records data at multiple observation points along the survey profile. The profiling, therefore, helps in investigating lateral conductivity variations in the model along the x-direction. In this case, it results in $N_\mathrm{d} = 129$ ERT data recording by using $N_\mathrm{e} = 32$ electrodes placed uniformly at every $1 \, \mathrm{m}$

320   from $x = -15.5 \, \mathrm{m}$ to $x = 15.5 \, \mathrm{m}$.
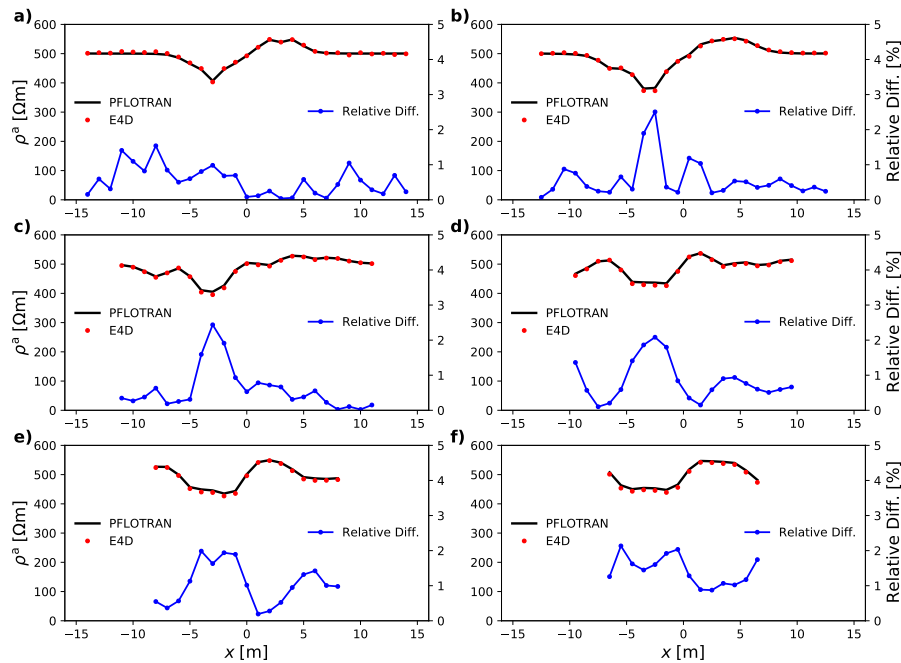
Figure 6. Apparent resistivity ρ^a responses computed for the 3D earth resistivity model in Fig. 5 using the Wenner configuration with spacings: (a) $a = 1 \, \mathrm{m}$, (b) $a = 2 \, \mathrm{m}$, (c) $a = 3 \, \mathrm{m}$, (d) $a = 4 \, \mathrm{m}$, (e) $a = 5 \, \mathrm{m}$, and (f) $a = 6 \, \mathrm{m}$ (upper plots). They are calculated using PFLOTRAN (solid black lines) and E4D (filled red circles) for an ERT profiling along a survey profile at $y = z = 0$ from $x = -16 \, \mathrm{m}$ to $x = 16 \, \mathrm{m}$. The lower plots (blue lines) show the relative difference (in percentage) between PFLOTRAN and E4D results.

The main computational domain is discretized with a uniform grid spacing of $0.2 \, \mathrm{m}$ in all the three directions, while the boundary domain is again discretized with severely stretched non-uniform grid spacings. The model discretization leads to a grid with $200 \times 120 \times 60$ FV cells and, hence, $1,440,000$ DOFs in the corresponding system of linear equations. PFLOTRAN simulated the ERT profiling data using 128 processing cores on Deception. Total simulation time was $9 \, \mathrm{s}$.

325   Figures $6(a) - (f)$ (upper curves) show the apparent resistivity ρ^{a} responses computed for the 3D model in Fig. 5 using the
ERT profiling with the Wenner configuration, respectively, with electrode spacings of 1, 2, 3, 4, 5, and, 6 m. The solid black
lines show the responses computed using PFLOTRAN. All responses exhibit the characteristics of the conductive and resistive
anomalous blocks embedded in a homogeneous background of conductivity $0.002\,\mathrm{Sm}^{-1}$ or resistivity $500\,\Omega\mathrm{m}$; see, e.g., the
low apparent resistivity on the left and high apparent resistivity on the right sides of the plots. These responses are compared

330   against responses computed using E4D (Johnson et al., 2010; Johnson and Wellman, 2015). In E4D, an unstructured-mesh FE
method is implemented to perform the forward modeling. The filled red circles show the responses computed using E4D. The
relative differences between the two codes are shown by the lower blue lines, which vary from 0.02% to 2.5%. The average
relative difference ϵ computed using Eq. (30) is 0.77%. These relatively small differences imply a good agreement between
responses computed using both codes.

6   Inversion results

To examine the efficiency of PFLOTRAN to invert ERT data, we consider a model modified from Fig. 5 by cropping the model
for $|x| > 8$ m. The modified model, therefore, has the dimension of $16 \times 16 \times 8\,\mathrm{m}^{3}$. The model is discretized using the same
grid spacings as in the previous 3D modeling example, which resulted in $120 \times 120 \times 60 = 864,000$ FV cells. We computed
synthetic ERT data for three survey lines located at the ground surface at $y = -5$ m, $y = 0$ m, and $y = 5$ m from $x = -8$ m to

340    $x = 8$ m. Electrodes are placed uniformly with an electrode spacing of 1 m along the three survey lines from $x = -7.5$ m to
$x = 7.5$ m, i.e., 16 electrodes along each survey line. Using these $N_{e} = 48$ electrodes, ERT data were simulated considering
different combinations of a set of 4 electrodes, where 2 electrodes acted as the current and the remaining 2 as the potential
receiving electrodes. These electrode combinations result in $N_{d} = 2070$ simulated ERT data. PFLOTRAN simulated these
ERT data using 128 processing cores on Deception. Total simulation time was 6 s. In this case, ERT data were simulated in the

345   form of the resistance obtained using $\frac{\Delta\phi}{I}$, which basically equals to the potential difference $\Delta\phi$ for unit current ($I = 1$ A).

The simulated ERT data were then inverted using PFLOTRAN starting with a model having a half-space conductivity of
$0.0022\ \mathrm{Sm}^{-1}$. The starting model conductivity was obtained by averaging the apparent conductivity computed from the given
ERT data. The previously described modeling grid also acted as the inversion grid, i.e., each cell in the model was used as an
inversion parameter. Therefore, we needed to invert for $N_{m} = 864,000$ model parameters. PFLOTRAN inverted the ERT data

350   using 512 processing cores on Deception. Total inversion time was 74 s.

Figure 7 shows the inverted conductivity model. The inverted model agrees well with the true model: the inversion recovered
the conductive and resistive anomalies in the model. The inverted resistivity, however, varies smoothly in the model because
a smooth regularization constraint is applied by minimizing the difference of the cell conductivity and the conductivity of its
neighboring cells. Further discussion on the implementation of our regularization schemes is beyond the scope of the current

355   paper.

The initial chi-squared data misfit χ^{2} was 14.8. As the inversion progressed, χ^{2} decreased as shown in Fig. 8. The inversion
took 11 iterations to satisfy the convergence criteria defined by $\chi^{2} \leq 0.9$. To further examine the efficiency of PFLOTRAN
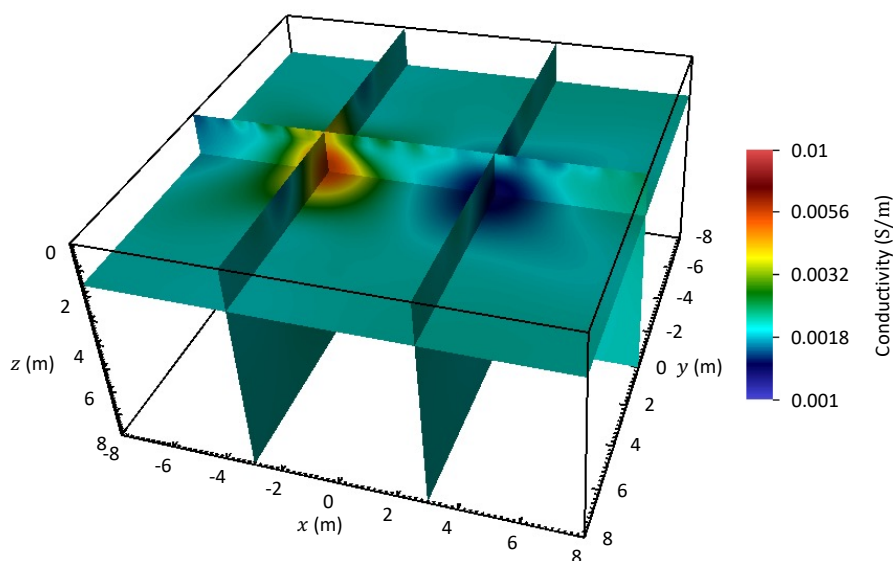
Figure 7. Inversion result of the simulated ERT data for a model modified from Fig. 5 by cropping the model for $|x| > 8$ m.
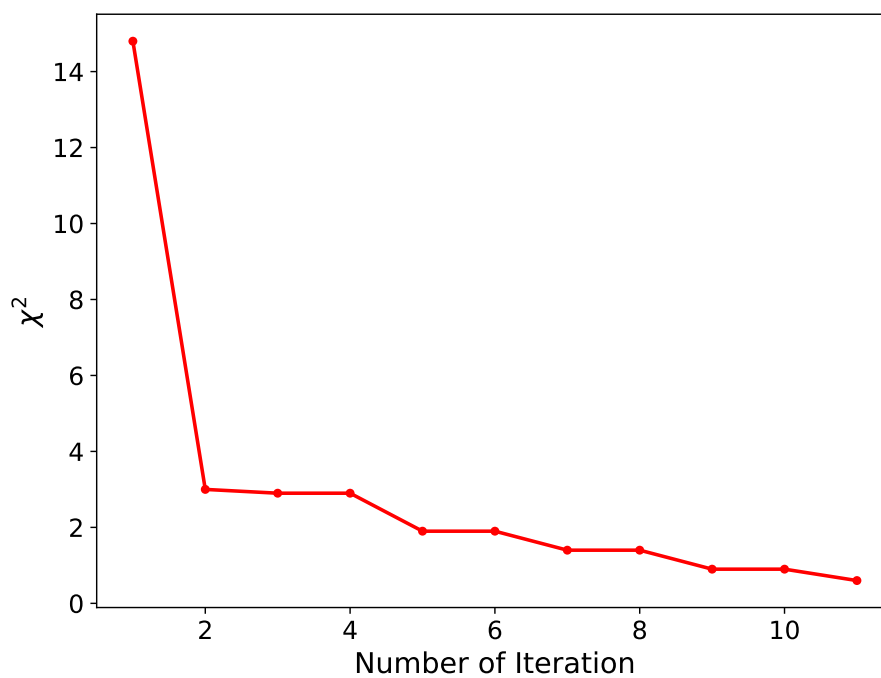
Figure 8. A measure of data misfit as the inversion progresses: χ^2 versus Number of Iteration.
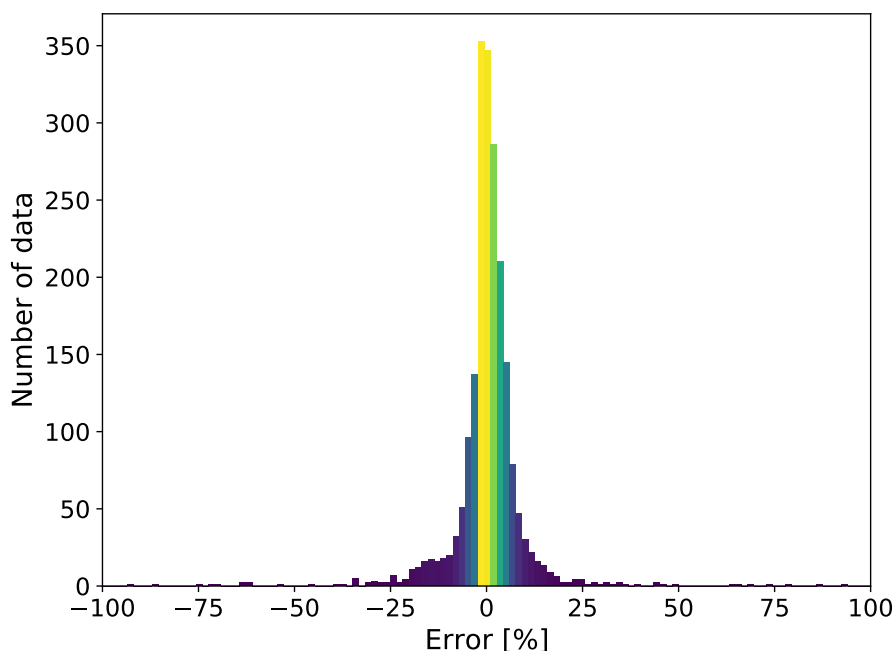
Figure 9. Histogram of data-fit error, which is defined as ratio of the residual resistance (difference of the observed and predicted resistances) and observed resistance expressed as a percentage.

to fit the individual ERT data, a histogram of data-fit error is also shown in Fig. 9. The data-fit error is defined as ratio of the residual resistance (difference of the observed and predicted resistances) and observed resistance expressed as a percentage.

360   The histogram implies that the ERT data were fitted comparatively well.

7   Scalability tests

As discussed earlier, there are mainly two computationally intensive steps to invert ERT data: forward modeling and Jacobian computation. To demonstrate the parallel performance of PFLOTRAN for these two steps, large-scale scalability tests are performed in this section by using up to $1,024$ cores on the Deception Supercomputer or up to $131,072$ cores on the Theta

365   Supercomputer. Configuration details for Deception were previously given in the Modeling Banchmarking Results section (5). On the other hand, Theta is a leadership-class supercomputer housed at the Argonne Leadership Computing Facility (ALCF) at Argonne National Laboratory (www.alcf.anl.gov/alcf-resources/theta). With a peak performance of 11.7 PFLOPs, it is composed of $4,392$ compute nodes connected through the Cray Aries network interconnect. Each node has 64-core Intel Xeon Phi 7230 processors running at 1.3 GHz with 192 GB of memory. Therefore, there are $281,088$ computing cores available

370   on Theta.

Table 1. Test matrices obtained by rediscretizing the three-layer earth model in Fig. 3 using different cell sizes dx, dy, and dz in the x-, y-, and z-directions. N_x, N_y, and N_z are respectively the number of FV cells in the x-, y-, and z-directions. Note that the cell sizes are given only for the main computational domain; the boundary domain is discretized using severely stretched non-uniform cell sizes.

Matrix Name	Discretization				DOFs
	$dx = dy$ (m)	dz (m)	$N_x = N_y$	N_z	
$M2$	4.0	1.00	140	120	$2,352,000$
$M7$	2.0	1.00	240	120	$6,912,000$
$M19$	1.6	0.50	290	220	$18,502,000$
$M35$	1.6	0.25	290	420	$35,322,000$
$M64$	0.8	0.50	540	220	$64,152,000$
$M122$	0.8	0.25	540	420	$122,472,000$

To optimize performance, PETSc and PFLOTRAN compilations on Deception and Theta were linked to the Intel Math Kernel Library (MKL) for Basic Linear Algebra Subprograms (BLAS), Linear Algebra Package (LAPACK), and Scalable LAPACK. Moreover, the analysis is carried out on for the distributed-memory architectures using the message passing interface (MPI). Therefore, the multi-threading capability of Intel MKL libraries for shared-memory architectures was not exploited for the scalability analysis.

7.1 Forward modeling scalability

The three-layer earth model in Fig. 3 is first rediscretized to generate several test matrices for the analysis. Table 1 summarizes details of the test matrices $M2$, $M7$, $M19$, $M35$, $M64$, and $M122$ along with the number of DOFs in the governing matrix equations that ranges between 2 and 122 million. The naming of these matrices is based on the number of DOFs they represent, e.g., $M19$ represents a matrix equation with about 19 million DOFs. To the best of our knowledge, the modeling with 122 million DOFs stands as the largest ERT modeling reported in the geophysical literature. Having capability to solve for hundreds of millions DOFs efficiently is a crucial requirement for next-generation industry-scale ERT modeling and inversion problems.

Considering the six test matrices above, we performed the forward modeling scalability test on Theta for simulating ERT data for $N_e = 128$ electrodes, the same number of electrodes as in the three-layer benchmarking example. Figure 10 illustrates the PFLOTRAN ERT process model strong scaling for each test case (wall-clock time versus the number of processes employed). The wall-clock time is shown on the vertical axis, while the horizontal axis shows the number of computing cores; both axes are shown in logarithmic base 2 scale. For all the matrices, PFLOTRAN exhibits almost linear scalability on up to 8 192 cores. Beyond this, we notice a departure from the linear scaling. As discussed in Section 4, the departure can be explained by the deteriorating scalability of the linear solver used to solve the governing linear system (Eq. 10) on a very large number of cores ($> 10,000$ cores) due to the increasing cost of MPI global reduction operations. A detailed description of possible reasons for
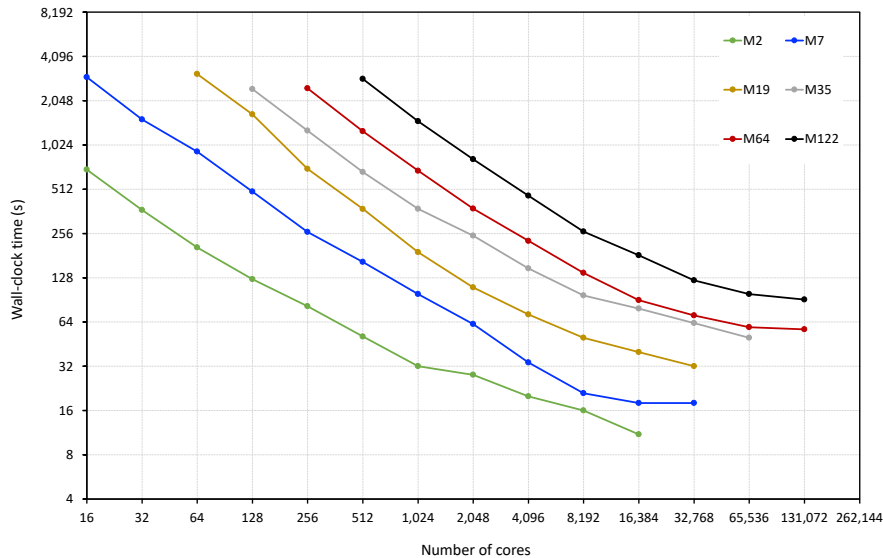
Figure 10. PFLOTRAN scalability for simulating ERT data for the model in Fig. 3 for $N_e = 128$ electrodes. The test is performed on the Theta Supercomputer considering six test matrices $M2$, $M7$, $M19$, $M35$, $M64$, and $M122$ with the respective number of DOFs of about 2, 7, 19, 35, 64, and 122 million (see Table 1 for details).

the departure from linear scaling in PFLOTRAN flow and transport is given by Hammond et al. (2012, 2014), most of which also applies to ERT simulation.

7.2 Jacobian computation scalability

395 To test the scalability of PFLOTRAN for the Jacobian computation, we consider a Jacobian matrix computed for inverting the ERT data in the Inversion Result Section 6. Recalling that $N_d = 2070$ ERT data and $N_m = 864,000$ model parameters for the inversion example, the dimension of the Jacobian matrix $\mathcal{J}$ is therefore $2070 \times 864,000$. The Jacobian matrix is computed at each inversion iteration after the forward modeling run and used in the normal equation (Eq. 15) to get a model update $\delta \mathbf{m}$.

The Jacobian scalability test is performed on the Deception Supercomputer. Figure 11 illustrates the strong scaling of PFLO-

400 TRAN wall-clock time for computing $\mathcal{J}$. It shows that PFLOTRAN exhibits linear (and sometimes superlinear) scalability for computing $\mathcal{J}$ with increasing numbers of cores. Consequently, the total wall-clock time for computing $\mathcal{J}$ using $1,024$ cores reduces to 0.5 s compared to 887 s when using a single core on Deception. The primary reason for this ideal scaling is based on the fact that all computations needed to build $\mathcal{J}$ are evenly distributed over each core in addition to no requirements of any MPI communications or global reductions.

405 For industry-scale ERT inversion problems, the perfectly linear scaling for computing $\mathcal{J}$ can be exploited to reduce the overall inversion wall-clock time even if PFLOTRAN exhibits deteriorating scalability for the forward modeling on a very
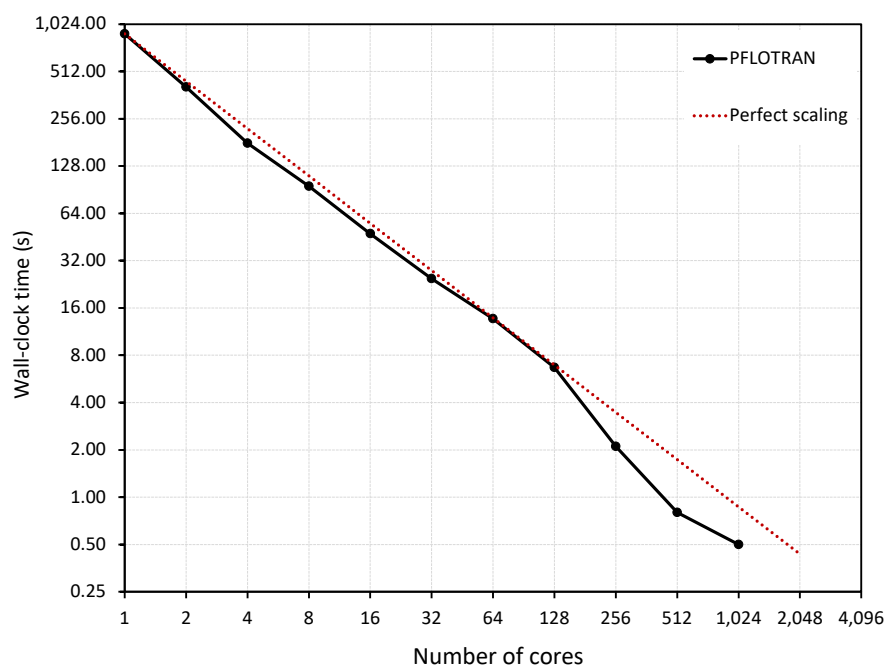
Figure 11. PFLOTRAN strong scaling for computing the Jacobian for the ERT inversion example in Fig. 7. The dimension of the Jacobian matrix $\mathcal{J}$ is $2070 \times 864,000$ and is distributed uniformly over each computing core.

large number of cores. However, one has to find an appropriate trade-off between forward modeling and Jacobian computation wall-clock times.

8   Conclusions

410   Two new capabilities — forward modeling and inversion of geophysical ERT data — are developed within PFLOTRAN, a massively parallel open-source, state-of-the-art, multi-phase, multi-component subsurface flow and transport simulation code. The capabilities are accurate, robust, and highly scalable on HPC platforms. Accuracy of the forward modeling capability was demonstrated for layered earth and 3D earth conductivity models by comparing our numerical results against well-established analytical and numerical results. The average relative differences stayed within a percent, demonstrating the high degree of

415   accuracy of the PFLOTRAN ERT process model. The inversion capability was demonstrated for a 3D synthetic case by recovering the conductivity of the model. Large-scale scalability tests illustrated that the forward modeling for models with hundreds of millions DOFs can be performed in a few minutes, e.g., ERT modeling for a model with 122 million DOFs and 122 electrodes was performed in $128\,\mathrm{s}$ by using $32,768$ cores of a supercomputer. The Jacobian computation, a key ingredient for the inversion, exhibited perfectly linear scaling, and as a result a Jacobian of $2070 \times 864,000$ dimension was computed in

420   $0.5\,\mathrm{s}$ using $1,024$ cores compared to $887\,\mathrm{s}$ using a single core. Moreover, integration of geophysical ERT capabilities within

PFLOTRAN opens door to perform coupled hydro-geophysical modeling and inversion, which is the focus of our future research.

Code and data availability. The source code, input file, and results presented in this manuscript are based on PFLOTRAN version v4.0. It can be downloaded from its Git repository at https://bitbucket.org/pflotran/pflotran and compiled after checking out the v4.0 tag (git

425 checkout maint/v4.0) following the instructions provided at https://pflotran.org/documentation. A snapshot of PFLOTRAN v4.0 is also uploaded to Zenodo repository at https://doi.org/10.5281/zenodo.6191926 (Jaysaval et al., 2022). The corresponding version of PETSc is v3.16.4 and was configured with Intel C/C++ 2020u4 using the following configuration script: ./configure –CFLAGS='-O3' –CXXFLAGS='-O3' –FFLAGS='-O3' –with-debugging=no –download-mpich=yes –download-hdf5=yes –download-fblaslapack=yes –download-metis=yes –download-parmetis=yes –download-hdf5-fortran-bindings=yes. The modeling and inversion results presented in the paper are also avail-

430 able at the above Zenodo repository in paper-examples folder. Each subfolder within it contains a README file with brief instructions to reproduce the results.

Author contributions. PJ implemented the ERT modeling and inversion capabilities with contributions from GEH. PJ performed the tests, analyzed the results, and prepared the figures. TCJ supervised the study. PJ wrote the paper with contributions from GEH, and all co-authors read and helped with editing.

435 *Competing interests.* The authors have no relevant financial or non-financial interests to disclose.

Acknowledgements. The research described in this paper is part of the INSITE (INduced Spectral Imaging for The Environment) Agile investment at Pacific Northwest National Laboratory (PNNL). It was conducted under the Laboratory Directed Research and Development Program at PNNL, a multiprogram national laboratory operated by Battelle for the U.S. Department of Energy (DOE). We gratefully acknowledge computing resources available through Research Computing at PNNL and Argonne Leadership Computing Facility (ALCF).

440 ALCF is a DOE Office of Science User Facility supported under Contract DE-AC02-06CH11357.

References

Alshehri, F. and Abdelrahman, K.: Groundwater resources exploration of Harrat Khaybar area, northwest Saudi Arabia, using electrical resistivity tomography, Journal of King Saud University-Science, 33, 101 468, 2021.

Badmus, B. and Olatinsu, O.: Geoelectric mapping and characterization of limestone deposits of Ewekoro formation, southwestern Nigeria, Journal of Geology and Mining Research, 1, 008–018, 2009.

Balay, S., Abhyankar, S., Adams, M. F., Brown, J., Brune, P., Buschelman, K., Dalcin, L., Dener, A., Eijkhout, V., Gropp, W. D., Kaushik, D., Knepley, M. G., May, D. A., McInnes, L. C., Mills, R. T., Munson, T., Rupp, K., Sanan, P., Smith, B. F., Zampini, S., Zhang, H., and Zhang, H.: PETSc Users Manual, Tech. Rep. ANL-95/11 - Revision 3.15, Argonne National Laboratory, 2021.

Bery, A. A., Saad, R., Mohamad, E. T., Jinmin, M., Azwin, I., Tan, N. A., and Nordiana, M.: Electrical resistivity and induced polarization data correlation with conductivity for iron ore exploration, The Electronic Journal of Geotechnical Engineering, 17, 3223–3233, 2012.

Blanchy, G., Saneiyan, S., Boyd, J., McLachlan, P., and Binley, A.: ResIPy, an intuitive open source software for complex geoelectrical inversion/modeling, Computers & Geosciences, 137, 104 423, 2020.

Blome, M., Maurer, H., and Schmidt, K.: Advances in three-dimensional geoelectric forward solver techniques, Geophysical Journal International, 176, 740–752, 2009.

Caputo, R., Piscitelli, S., Oliveto, A., Rizzo, E., and Lapenna, V.: The use of electrical resistivity tomographies in active tectonics: examples from the Tyrnavos Basin, Greece, Journal of Geodynamics, 36, 19–35, 2003.

Cockett, R., Kang, S., Heagy, L. J., Pidlisecky, A., and Oldenburg, D. W.: SimPEG: An open source framework for simulation and gradient based parameter estimation in geophysical applications, Computers & Geosciences, 85, 142–154, https://doi.org/10.1016/j.cageo.2015.09.015, 2015.

Coggon, J.: Electromagnetic and electrical modeling by the finite element method, Geophysics, 36, 132–155, 1971.

Dahlin, T.: 2D resistivity surveying for environmental and engineering applications, First break, 14, 1996.

Dahlin, T.: The development of DC resistivity imaging techniques, Computers & Geosciences, 27, 1019–1029, 2001.

Dahlin, T. and Zhou, B.: A numerical comparison of 2D resistivity imaging with 10 electrode arrays, Geophysical prospecting, 52, 379–398, 2004.

Das, U. C.: Direct current electric potential computation in an inhomogeneous and arbitrarily anisotropic layered earthl, Geophysical Prospecting, 43, 417–432, https://doi.org/10.1111/j.1365-2478.1995.tb00260.x, 1995.

Dey, A. and Morrison, H. F.: Resistivity modeling for arbitrarily shaped three-dimensional structures, Geophysics, 44, 753–780, 1979.

Ellis, R. and Oldenburg, D.: The pole-pole 3-D Dc-resistivity inverse problem: a conjugategradient approach, Geophysical journal international, 119, 187–194, 1994.

Gabarrón, M., Martínez-Pagán, P., Martínez-Segura, M. A., Bueso, M. C., Martínez-Martínez, S., Faz, Á., and Acosta, J. A.: Electrical resistivity tomography as a support tool for physicochemical properties assessment of near-surface waste materials in a mining tailing pond (El Gorguel, SE Spain), Minerals, 10, 559, 2020.

Greggio, N., Giambastiani, B., Balugani, E., Amaini, C., and Antonellini, M.: High-resolution electrical resistivity tomography (ERT) to characterize the spatial extension of freshwater lenses in a salinized coastal aquifer, Water, 10, 1067, 2018.

Günther, T., Rücker, C., and Spitzer, K.: Three-dimensional modelling and inversion of DC resistivity data incorporating topography—II. Inversion, Geophysical Journal International, 166, 506–517, 2006.

Hammond, G., Valocchi, A., and Lichtner, P.: Application of Jacobian-free Newton-Krylov with physics-based preconditioning to biogeo-chemical transport, Advances in Water Resources, 28, 359–376, https://doi.org/https://doi.org/10.1016/j.advwatres.2004.12.001, 2005.

Hammond, G. E., Lichtner, P. C., Lu, C., and Mills, R. T.: PFLOTRAN: Reactive flow & transport code for use on laptops to leadership-class supercomputers, in: Groundwater Reactive Transport Models, edited by Zhang, F., Yeh, G.-T. G., and Parker, J. C., pp. 141–159, BENTHAM SCIENCE PUBLISHERS, https://doi.org/10.2174/978160805306311201010141, 2012.

Hammond, G. E., Lichtner, P. C., and Mills, R. T.: Evaluating the performance of parallel subsurface simulators: An illustrative example with PFLOTRAN, Water Resources Research, 50, 208–228, https://doi.org/10.1002/2012WR013483, 2014.

Hestenes, M. and Stiefel, E.: Methods of conjugate gradients for solving linear systems, Journal of Research of the National Bureau of Standards, 49, 409, https://doi.org/10.6028/jres.049.044, 1952.

Jahandari, H. and Farquharson, C. G.: A finite-volume solution to the geophysical electromagnetic forward problem using unstructured grids, Geophysics, 79, E287–E302, 2014.

Jaysaval, P., Shantsev, D., and de la Kethulle de Ryhove, S.: Fast multimodel finite-difference controlled-source electromagnetic simulations based on a Schur complement approach, GEOPHYSICS, 79, E315–E327, https://doi.org/10.1190/geo2014-0043.1, 2014.

Jaysaval, P., Hammond, G. E., and Johnson, T. C.: ERT modeling and inversion using PFLOTRAN v4.0, https://doi.org/10.5281/zenodo.6191926, 2022.

Johnson, T. C. and Wellman, D.: Accurate modelling and inversion of electrical resistivity data in the presence of metallic infrastructure with known location and dimension, Geophysical Journal International, 202, 1096–1108, 2015.

Johnson, T. C., Versteeg, R. J., Ward, A., Day-Lewis, F. D., and Revil, A.: Improved hydrogeophysical characterization and monitoring through parallel modeling and inversion of time-domain resistivity andinduced-polarization data, GEOPHYSICS, 75, WA27–WA41, https://doi.org/10.1190/1.3475513, 2010.

Johnson, T. C., Slater, L. D., Ntarlagiannis, D., Day-Lewis, F. D., and Elwaseif, M.: Monitoring groundwater-surface water interaction using time-series and time-frequency analysis of transient three-dimensional electrical resistivity changes, Water Resources Research, 48, 2012.

Karypis, G. and Schloegel, K.: METIS/ParMETIS Parallel Graph Partitioner, Tech. rep., https://www-users.cs.umn.edu/~karypis/metis/, accessed: 2021-11-11, 2013.

Kessouri, P., Johnson, T., Day-Lewis, F. D., Wang, C., Ntarlagiannis, D., and Slater, L. D.: Post-remediation geophysical assessment: Inves-tigating long-term electrical geophysical signatures resulting from bioremediation at a chlorinated solvent contaminated site, Journal of environmental management, 302, 113 944, 2022.

Lee, T.: An integral equation and its solution for some two-and three-dimensional problems in resistivity and induced polarization, Geophys-ical Journal International, 42, 81–95, 1975.

Li, Y. and Spitzer, K.: Three-dimensional DC resistivity forward modelling using finite elements in comparison with finite-difference solu-tions, Geophysical Journal International, 151, 924–934, 2002.

Loke, M., Chambers, J., Rucker, D., Kuras, O., and Wilkinson, P.: Recent developments in the direct-current geoelectrical imaging method, Journal of applied geophysics, 95, 135–156, 2013.

Lysdahl, A. K., Bazin, S., Christensen, C., Ahrens, S., Günther, T., and Pfaffhuber, A. A.: Comparison between 2D and 3D ERT inversion for engineering site investigations–a case study from Oslo Harbour, Near Surface Geophysics, 15, 201–209, 2017.

Martínez, J., Rey, J., Sandoval, S., Hidalgo, M., and Mendoza, R.: Geophysical prospecting using ERT and IP techniques to locate Galena veins, Remote Sensing, 11, 2923, 2019.

Méndez-Delgado, S., Gómez-Treviño, E., and Pérez-Flores, M.: Forward modelling of direct current and low-frequency electromagnetic
fields using integral equations, Geophysical Journal International, 137, 336–352, 1999.

Meyerhoff, S. B., Maxwell, R. M., Revil, A., Martin, J. B., Karaoulis, M., and Graham, W. D.: Characterization of groundwater and surface
water mixing in a semiconfined karst aquifer using time-lapse electrical resistivity tomography, Water Resources Research, 50, 2566–2585,
2014.

Mills, R. T., Hammond, G. E., Lichtner, P. C., Sripathi, V., Mahinthakumar, G., and Smith, B. F.: Modeling Subsurface Reactive Flows Using
Leadership-Class Computing, in: 5th Annual Conference of Scientific Discovery through Advanced Computing (SciDAC 2009), vol. 180
of *Journal of Physics Conference Series*, https://doi.org/10.1088/1742-6596/180/1/012062, 2009.

Nocedal, J. and Wright, S.: Numerical optimization, Springer Science & Business Media, 2006.

Park, S., Yi, M.-J., Kim, J.-H., and Shin, S. W.: Electrical resistivity imaging (ERI) monitoring for groundwater contamination in an uncon-
trolled landfill, South Korea, Journal of Applied Geophysics, 135, 1–7, 2016.

Park, S. K. and Van, G. P.: Inversion of pole-pole data for 3-D resistivity structure beneath arrays of electrodes, GEOPHYSICS, 56, 951–960,
https://doi.org/10.1190/1.1443128, 1991.

Penz, S., Chauris, H., Donno, D., and Mehl, C.: Resistivity modelling with topography, Geophysical Journal International, 194, 1486–1497,
2013.

Pervago, E., Mousatov, A., and Shevnin, V.: Analytical solution for the electric potential in arbitrary anisotropic layered media applying
the set of Hankel transforms of integer order, Geophysical Prospecting, 54, 651–661, https://doi.org/10.1111/j.1365-2478.2006.00555.x,
2006.

Ren, Z., Qiu, L., Tang, J., Wu, X., Xiao, X., and Zhou, Z.: 3-D direct current resistivity anisotropic modelling by goal-oriented adaptive finite
element methods, Geophysical Journal International, 212, 76–87, 2018.

Revil, A., Karaoulis, M., Johnson, T., and Kemna, A.: Some low-frequency electrical methods for subsurface characterization and monitoring
in hydrogeology, Hydrogeology Journal, 20, 617–658, 2012.

Richards, K., Revil, A., Jardani, A., Henderson, F., Batzle, M., and Haas, A.: Pattern of shallow ground water flow at Mount Princeton Hot
Springs, Colorado, using geoelectrical methods, Journal of Volcanology and Geothermal Research, 198, 217–232, 2010.

Rizzo, E., Colella, A., Lapenna, V., and Piscitelli, S.: High-resolution images of the fault-controlled High Agri Valley basin (Southern Italy)
with deep and shallow electrical resistivity tomographies, Physics and Chemistry of the Earth, Parts A/B/C, 29, 321–327, 2004.

Rockhold, M. L., Robinson, J. L., Parajuli, K., Song, X., Zhang, Z., and Johnson, T. C.: Groundwater characterization and monitoring at a
complex industrial waste site using electrical resistivity imaging, Hydrogeology Journal, 28, 2115–2127, 2020.

Rosales, R. M., Martínez-Pagan, P., Faz, A., and Moreno-Cornejo, J.: Environmental monitoring using electrical resistivity tomography
(ERT) in the subsoil of three former petrol stations in SE of Spain, Water, Air, & Soil Pollution, 223, 3757–3773, 2012.

Rücker, C., Günther, T., and Spitzer, K.: Three-dimensional modelling and inversion of dc resistivity data incorporating topography—I.
Modelling, Geophysical Journal International, 166, 495–505, 2006.

Rücker, C., Günther, T., and Wagner, F. M.: pyGIMLi: An open-source library for modelling and inversion in geophysics, Computers &
Geosciences, 109, 106–123, 2017.

Rucker, D. F., Myers, D. A., Cubbage, B., Levitt, M. T., Noonan, G. E., McNeill, M., Henderson, C., and Lober, R. W.: Surface geophysical
exploration: developing noninvasive tools to monitor past leaks around Hanford's tank farms, Environmental monitoring and assessment,
185, 995–1010, 2013.

Schulz, R.: The method of integral equation in the direct current resistivity method and its accuracy, Journal of geophysics, 56, 192–200, 1985.

Singha, K., Johnson, T. C., Day-Lewis, F. D., and Slater, L. D.: Electrical Imaging for Hydrogeology, The Groundwater Project, Guelph, Ontario, Canada, 2022.

555 Slater, L.: Near surface electrical characterization of hydraulic conductivity: From petrophysical properties to aquifer geometries—A review, Surveys in Geophysics, 28, 169–197, 2007.

Spitzer, K.: A 3-D finite-difference algorithm for DC resistivity modelling using conjugate gradient methods, Geophysical Journal International, 123, 903–914, 1995.

Storz, H., Storz, W., and Jacobs, F.: Electrical resistivity tomography to investigate geological structures of the earth's upper crust, Geophysical prospecting, 48, 455–472, 2000.

560

Uhlemann, S., Chambers, J., Falck, W. E., Tirado Alonso, A., Fernández González, J. L., and Espín de Gea, A.: Applying electrical resistivity tomography in ornamental stone mining: challenges and solutions, Minerals, 8, 491, 2018.

Zhang, J., Mackie, R. L., and Madden, T. R.: 3-D resistivity forward modeling and inversion using conjugate gradients, Geophysics, 60, 1313–1325, 1995.

565 Zhdanov, M. S. and Keller, G. V.: The geoelectrical methods in geophysical exploration, Methods in geochemistry and geophysics, 31, I–IX, 1994.